PCCP

Influence of H- and OH-adsorbates on the ethanol oxidation reaction – A DEMS Study

SCHOLARONE™
Manuscripts

Journal Name

Dynamic Article Links ▶

ARTICLE TYPE

Influence of H- and OH-adsorbates on the ethanol oxidation reaction – A DEMS Study

Antoine Bach Delpeuch*[a,b], Marian Chatenet[b,c, #], Maria Sol Rau[a], Carsten Cremers[a]

The ethanol oxidation reaction (EOR) was investigated by potentiodynamic techniques on Pt/C, Rh/C, Pt-Rh/C, Pt-SnO$_2$/C and Pt-Rh-SnO$_2$/C by differential electrochemical mass spectrometry (DEMS) in a flow cell system. Prior to the cyclic voltammetries, adsorption of H- and OH-species was carried out by 10 chronoamperometry at E_{ad} = 0.05 and 1 V *vs.* RHE, respectively, in order to examine their influence on the EOR on the different electrocatalysts. For the sake of comparison, another adsorption potential was chosen at E_{ad} = 0.3 V *vs.* RHE, in the double layer region (*i.e.* in the absence of such adsorbates). For this study, 20 wt.% electrocatalysts were synthesized by a modified polyol method and were physically characterized by inductively coupled plasma atomic emission spectrometry (ICP-AES), X-ray diffraction 15 (XRD) and transmission electron microscopy (TEM). When comparing the first and second cycles of the cyclic voltammograms (CVs) on Pt/C and Pt-SnO$_2$/C, the H$_{ad}$ presence on the electrocatalysts surface seems to hinder the initiation of the ethanol electrooxidation, whereas the reaction onset potential is shifted negatively with the presence of OH-adsorbates. In contrast to them, the EOR on Rh/C is enhanced when the electrocatalyst surface is covered with H$_{ad}$ and is inhibited after adsorption at E_{ad} = 0.3 and 1 V 20 *vs.* RHE. Finally, on Pt-Rh/C and Pt-Rh-SnO$_2$/C, neither the H- nor OH-adsorbates do impact the EOR initiation. The lowest EOR onset was recorded on Pt-SnO$_2$/C and Pt-Rh-SnO$_2$/C electrocatalysts. The CO$_2$ currency efficiency (CCE) was also determined for each electrocatalyst and demonstrated higher values on Pt-Rh-SnO$_2$/C.

Introduction

25 Direct ethanol fuel cell (DEFC) has received growing attention as renewable power source over the past few years [1–6]. Besides ethanol fuel non toxicity, its facile production by biomass fermentation and its ease of storage, transportation and delivery with the existing infrastructure, ethanol high theoretical energy 30 density makes it highly attractive especially for mobile applications. Nonetheless, the sluggish kinetics of the ethanol oxidation reaction (EOR) and its low selectivity toward its complete oxidation into CO$_2$ (12 electrons) constitute major obstacles for DEFC commercialization [7–11]. The total 35 electrooxidation of ethanol into CO$_2$ is compromised by the difficult cleavage of the C-C bond. As a result, ethanol oxidation operates through parallel pathways and may partially yield acetaldehyde (2 electrons) and acetic acid (4 electrons) [4,12–14].

The EOR has been largely reviewed so far on bulk Pt and Pt/C 40 [4,10,15–20]. A relative consensus exists concerning the limited ethanol conversion into CO$_2$ in acidic medium at room temperature. The so-called CO$_2$ current efficiency (CCE), which is a quantification of the current generated during the ethanol total oxidation into CO$_2$ reported to the EOR overall current, is 45 generally found between 5 and 20% depending on the operating conditions [10,21–23]. Besides, the EOR on Pt bulk and Pt/C electrocatalysts suffers from a high onset overpotential, which is thought to originate from the difficult ethanol adsorption on the electrocatalyst surface at low potentials [24,25], as also observed for 50 methanol [26,27].

The development of bi- and tri-metallic Pt-based electrocatalysts has been emphasized during the past decades in order to overcome these issues: Pt-Ru/C [28–30], Pt-Rh/C [11,31,32], Pt-SnO$_2$/C [1,8,33], Pt-Rh-SnO$_2$/C [34,35], Pt-Ir-SnO$_2$/C [36], Pt-Ru-Mo/C [37], 55 Pt-Sn-Mo/C [38]… Differential electrochemical mass spectrometry (DEMS) investigations have shown promising results in the C-C bond breaking by rhodium metal [39,40]. Nonetheless, EOR studies on Pt-Rh/C bi-metallic electrocatalyst shows some controversies: some of them show a higher CCE on Pt-Rh/C than on Pt/C [22,41,42], 60 while others demonstrate similar performances regarding the C-C bond splitting [21]. The lower EOR onset potential on Pt-Rh/C electrocatalyst compared to Pt/C is however generally admitted [21,22,25,41–43]. A reason could be the better dehydrogenation of the ethanol molecule at low potentials on Pt-Rh/C than on Pt/C [25].

65 Pt-SnO$_2$/C is also a well investigated bi-metallic electrocatalyst for the EOR [1,8,33,44]. Adding tin to the electrocatalyst material leads to a negative shift of the EOR onset potential and also enhances the selectivity of the ethanol electrooxidation toward

acetic acid formation [9,44,45]. This enhanced electroactivity is accounted for by a bi-functional mechanism between Pt and SnO_2 moieties, in which the oxophilic character of tin enables OH_{ad}-species formation from water dissociation at lower potential, these species favouring the further oxidation of adsorbed acetaldehyde into acetic acid [46]. However, even with this positive effect, the CO_2 current efficiency recorded on Pt-SnO_2/C does not differ significantly to that on Pt/C [8,44].

The EOR on tri-metallic Pt-Rh-SnO_2/C electrocatalyst demonstrated a large negative shift of the onset potential as well as a higher activity compared to Pt/C and Pt-Rh/C [34,47–49]. According to one of these studies [48], while the C-C bond cleavage would be assured by rhodium and the ethanol dehydrogenation by platinum, the OH_{ad}-species necessary for the further oxidation of the products of the C-C bond cleavage (CO_{ad}) into CO_2 would be provided by SnO_2. This synergetic effect between the three metals/oxides would facilitate the complete ethanol oxidation into CO_2.

In the present study, the influence of pre-adsorbed hydrogen and hydroxide species on the ethanol oxidation reaction (EOR) has been investigated on home-made model EOR electrocatalysts (Pt/C, Rh/C, Pt-Rh/C, Pt-SnO_2/C and Pt-Rh-SnO_2/C). The H- and OH-adsorbates were formed by potentiostatic hold at $E_{ad} = 0.05$ and 1 V *vs.* RHE respectively, whereas "water adsorbates-free" surfaces were prepared by potentiostatic hold at $E_{ad} = 0.3$ V *vs.* RHE. The home-made model electrocatalysts were firstly characterized by thermogravimetric analysis (TGA), inductively coupled plasma atomic emission spectrometry (ICP-AES), powder X-ray diffraction (XRD) and transmission electron microscopy (TEM) to determine the metal-to-carbon ratio and metal crystallite/nanoparticles size and distribution on the carbon support. The EOR was thoroughly studied by Differential Electrochemical Mass Spectrometry (DEMS) using the mass-to-charge signals *m/z* 22, *m/z* 29 and *m/z* 61, which are representative of CO_2, acetaldehyde and ethyl acetate formation respectively. The latter, product of the esterification of acetic acid with ethanol, is an indirect proof of the formation of acetic acid during the electrochemical reactions [50]. For this reason, the authors have decided to analyse the variations of the signal *m/z* 61 for the acetic acid production. Finally, the CO_2 current efficiency (CCE) during the electrooxidation reactions was determined after calibration of the mass-to-charge signal *m/z* 22.

Experimental

Materials preparation

Carbon-supported Pt/C, Rh/C, Pt-Rh/C, Pt-SnO_2/C, Pt-Rh-SnO_2/C, with 20 wt.% overall metal load, were prepared using a modified polyol method. In a typical procedure, the calculated amount of metal precursors, H_2PtCl_6 (Aldrich), $RhCl_3.xH_2O$ and $SnCl_2$, was dissolved in a solution containing water and ethylene glycol (EG) (volume ratio 2:1), prior to the addition of carbon black particles (Vulcan XC-72R, Cabot) dispersed in an EG solution by sonication. The pH of the whole solution was subsequently adjusted to 12 using a 0.5 M NaOH solution (diluted in EG) and let under stirring for one hour at ambient temperature. Thereafter the solution was heated up to 160 °C, maintained at this temperature for three hours and cooled down

overnight. The pH of the solution was then fixed to 3 using a 0.5 M H_2SO_4 aqueous solution and stirred for 24 h. Finally, the electrocatalyst powder was filtrated, washed copiously with distilled water and dried overnight in an oven at 80 °C.

Physico-chemical characterizations

The metal-carbon ratio in the electrocatalysts was checked by thermogravimetric analysis (TGA, Q 5000 from TA Instruments), while the composition of the bi- and tri-electrocatalysts (metal-metal ratio) was determined by ICP-AES (iCAP 6300 Thermo). The crystalline structure and average size of the metal nanoparticles was analyzed by powder X-ray diffraction (XRD, Bruker AXS D8) in the 2θ range from 15° to 90° using Cu Kα radiation with a scan rate of 0.74° min^{-1}. The electrocatalyst morphology was studied by transmission electron microscopy (TEM, Jeol 2010), and the nanoparticle size distribution (PSD) reconstructed using representative micrographs (*ca*. 400 nanoparticles being counted in average for the construction of each PSD histogram). The PSD was used to determine the number-averaged d_N, surface-averaged d_S and volume-averaged d_V diameters of the nanoparticles:

$$d_N = \sum_i \frac{n_i d_i}{n_i} \tag{1}$$

$$d_S = \sum_i \frac{n_i d_i^3}{n_i d_i^2} \tag{2}$$

$$d_V = \sum_i \frac{n_i d_i^4}{n_i d_i^3} \tag{3}$$

where n_i is the number of particles of diameter d_i.

Electrochemical measurements

The DEMS measurements were performed in a flow cell system described elsewhere [51]. The working electrode was prepared from a uniform ink of the prepared electrocatalyst and supported on a thin Gore-Tex PTFE membrane (60 μm thickness, 0.02 μm mean pore size, 50% porosity) baring a thin, porous and electrocatalytically inert (with respect to the EOR) sputtered Au layer. The ink was composed of 3 mg of electrocatalyst dispersed by sonication in a 400 μL mixture of isopropanol and water (volume ratio 3:1). The electrocatalyst thin-film was prepared by pipetting 36 μL of the ink onto the sputtered Au/PTFE membrane (1 cm^2 geometric area), so as to form a uniform layer (87.5 μg cm^{-2}). Nafion® was used as ionomer to stabilize the catalytic particles on the electrode surface. The amount of Nafion® was always added on the electrocatalytic particles so that it amounts 50 wt.% of the total electrocatalyst. The counter electrode was a platinum foil and the reference electrode a reversible hydrogen electrode (RHE). The activation of the electrocatalyst, as well as the stripping experiments, was carried out in 0.5 M H_2SO_4 supporting (aqueous) electrolyte while the ethanol oxidation reaction (EOR) was carried out in 0.5 M H_2SO_4 + 0.1 M EtOH.

The electrochemical tests were run using a GAMRY Reference 3000 potentiostat connected to a Balzers QMS 200 mass spectrometer. For the sake of comparison, the electrochemical results presented hereafter are normalized by the metal mass at the working electrode.

CO stripping experiments were preceded by a chronoamperometry (CA) at $E_{ad} = 0.15$ V *vs.* RHE. During the
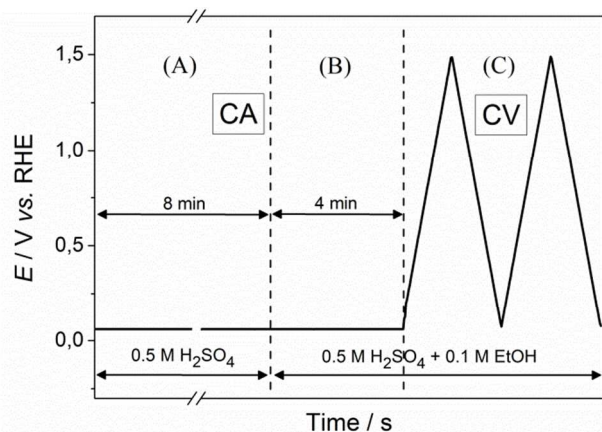
Fig.1 Potential *vs.* time representation of (A) the adsorbates adsorption in 0.5 M H_2SO_4 (represented here at 0.05 V *vs.* RHE), (B) the solution change in 0.5 M H_2SO_4 + 0.1 M EtOH and (C) the potentiodynamic ethanol oxidation reaction starting at 0.2 V *vs.* RHE.

Fig.2 XRD pattern of carbon supported Pt/C, Rh/C, Pt-Rh/C, Pt-SnO$_2$/C and Pt-Rh-SnO$_2$/C electrocatalysts prepared by Polyol method.

first 8 min of the CA, the electrolyte flowing through the cell was saturated with CO by bubbling CO in the reservoir in order to saturate the surface of the electrocatalysts with CO_{ad}. After that, the solution in the reservoir was purged with Ar during 20 min until the end of the CA to remove remaining dissolved CO from the cell. Finally, the stripping cyclic voltammetry (CV) was applied.

Similarly, prior to the potentiodynamic voltammetries presented hereafter, adsorption of hydrogen and hydroxide species on the electrocatalysts surface was carried out in a 0.5 M H_2SO_4 base electrolyte flowing through the cell containing the working electrode during 8 min at E_{ad} = 0.05 and 1 V *vs.* RHE respectively. The solution was then switched to 0.5 M H_2SO_4 + 0.1 M EtOH during 4 min so as to allow a stabilization of the ionic baseline for the studied mass-to-charge signals before the following CVs started (Fig. 1). For the sake of comparison, CVs carried out after a CA at E_{ad} = 0.3 V *vs.* RHE were also investigated, as this potential is located in the so-called double layer region which should prevent any hydrogen or hydroxide adsorption (water adsorbates-free electrode).

Calibration of the mass spectrometer

A calibration of the mass-to-charge signal *m/z* 22 regarding the corresponding faraday current was primordial in order to quantify the current generated during the total ethanol oxidation into CO_2 detected by the DEMS [52]. For that purpose, the CO stripping is used as calibration reaction, as it is a well-known reaction involving only the production of CO_2 (4):

$$CO_{ad} + H_2O \rightarrow CO_2 + 2H^+ + 2e^- \tag{4}$$

The mass-to-charge signal *m/z* 22 is the only signal in the present experimental conditions (oxidation of ethanol) that can be ascribed solely to the production of CO_2 (doubly ionized $[CO_2^{++}]$). Indeed, the signal *m/z* 44 (ionized $[CO_2^+]$) is compromised by the presence of acetaldehyde (ionized $[CH_3CHO^+]$), a well-known by-product of the EOR.

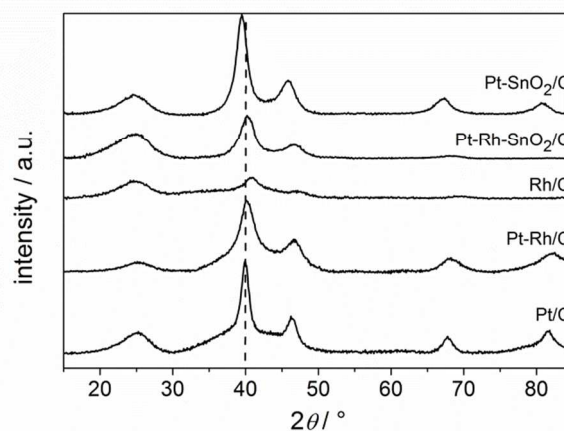Equation (5) correlates the ionic current for the mass-to-charge signal *m/z* 22 and the faradaic current:

$$K_{22}^* = \frac{2\, I_{m/z\,22,CO}}{I_{f,CO}} \tag{5}$$

where $I_{m/z\,22,co}$ is the ionic charge of the mass-to-charge signal *m/z* 22, $I_{f,co}$ the faradaic charge, 2 the number of electrons exchanged during the electrooxidation of adsorbed CO in CO_2 and K_{22}^* the calibration constant of the signal *m/z* 22.

The CO_2 current efficiency (CCE) can then be deduced using the faradaic and ionic current values obtained during the ethanol oxidation:

$$CCE = \frac{6}{K_{22}^*} \frac{I_{m/z\,22}}{I_f} \tag{6}$$

with 6 the average number of electrons exchanged for the production of one CO_2 molecule.

Results and discussion

Physical characterization

Representative XRD spectra of the carbon-supported Pt/C, Rh/C, Pt-Rh/C, Pt-SnO$_2$/C and Pt-Rh-SnO$_2$/C electrocatalysts are displayed in Fig. 2. The sharpness of Pt/C and Pt-Rh-SnO$_2$/C patterns show well crystallized nanoparticles. The diffraction peaks of Pt/C at *ca.* 40, 46.5, 67.8, 82, 86 are assigned respectively to the (111), (200), (220), (311), (222) planes, characteristic of a face-centered cubic (fcc) structure. Rh/C and Pt-based bi- and tri-metallic electrocatalysts were also found to crystallize in the fcc structure. An evaluation of the average particle size was carried out using the Scherrer's law on the (220) diffraction peak. The lattice parameters and the average particle sizes are summarized in Table 1.

Pt/C and Rh/C are loaded at 20 wt.% and 21.1 wt.%, respectively, as revealed by TGA. ICP-AES analyses showed the presence of 17.07 wt.% Pt and 7.46 wt.% Rh for Pt-Rh/C (24.5 wt.% $Pt_1Rh_{0.8}$/C), 15.01 wt.% Pt and 2.69 wt.% SnO_2 for Pt-SnO$_2$/C (17.7 wt.% $Pt_1(SnO_2)_{0.8}$/C) and 13.38 wt.% Pt, 4.03 wt.% Rh and 2.73 wt.% SnO_2 for Pt-Rh-SnO$_2$/C (20.14 wt.% $Pt_1Rh_{0.58}(SnO_2)_{0.35}$/C).

The electrocatalysts morphology and the particle size distribution (PSD) were further characterized by TEM. Fig. 3 displays a uniform dispersion of relatively small nanoparticles on the carbon support for most of the electrocatalysts. Yet, the TEM

ARTICLE TYPE

Table 1 Structural proprieties of Pt/C, Rh/C, Pt-Rh/C, Pt-SnO$_2$/C and Pt-Rh-SnO$_2$/C electrocatalysts obtained by XRD and TEM

Electrocatalyst	Effective composition by ICP-AES	a / Å	d_{XRD} / nm	d_{Elec} / nm	d_N / nm	d_S / nm	d_V / nm
Pt/C	-	3.93	5.8	4.8	2.3	2.6	2.9
Rh/C	-	3.84	2.8	3.8	2.1	2.4	2.7
Pt-Rh/C	Pt$_1$Rh$_{0.8}$/C	3.91	3.5	4.2	2.3	3.3	3.9
Pt-SnO$_2$/C	Pt$_1$(SnO$_2$)$_{0.3}$/C	3.97	4.5	9.4	3.3	5.8	7.8
Pt-Rh-SnO$_2$/C	Pt$_1$Rh$_{0.58}$(SnO$_2$)$_{0.35}$/C	3.91	3.4	4.8	2.4	2.6	2.8

a: lattice parameter; d_{XRD}: mean nanoparticle size (XRD); d_{Elec}: electrochemical mean particle size; d_N: number-averaged diameter (TEM); d_S: surface-averaged diameter (TEM); d_V: volume-averaged diameter (TEM).

investigation on Pt-SnO$_2$/C revealed the presence of larger nanoparticles. The associated PSD histograms in Fig. 3 reveal a narrow particle size distribution with a very similar mean particle size for the electrocatalysts (from 2.1 to 2.4 nm), except for Pt-SnO$_2$/C (3.3 nm). The presence of some agglomerates was observed on Pt-Rh/C and to a larger extent on Pt-SnO$_2$/C.

The surface-averaged diameter d_s estimated from the PSD histograms can be compared to the mean particle size (d_{Elec}) calculated from the electrochemically active surface area (A) estimated from the charge of CO-stripping. Assuming the cuboctahedral shape of the nanoparticles, d_{Elec} can be calculated as followed:

$$d_{Elec} = \frac{6\left(3+\sqrt{3}\right)W_m}{5\,A_m\,\rho_m} \qquad (4)$$

with W_m the mass of deposited metal nanoparticles and ρ_m the metals density.

Table 1 points out a good correspondence between the TEM and XRD mean particle diameter, d_V and d_{XRD} respectively, for Pt/C, Rh/C and Pt-Rh-SnO$_2$/C whereas the presence of agglomerates on Pt-Rh/C and Pt-SnO$_2$/C explain the discrepancies. The inconsistency between d_{Elec} and d_s values for the multi-metallic electrocatalysts may also be explained by an alloy effect that impacts CO$_{ad}$ adsorption/electrooxidation and the resulting electrochemical active surface area (ECSA). More specifically, the ECSA from Pt-SnO$_2$/C and Pt-Rh-SnO$_2$/C may be underestimated (and thus d_{Elec} overestimated) due to CO$_{ad}$ electrooxidation probably occurring during the chronoamperometry at $E_{ad} = 0.15$ V $vs.$ RHE preceding the CV.

CV in base electrolyte

Fig. 4 presents cyclic voltammograms in supporting electrolyte (0.5 M H$_2$SO$_4$) on Pt/C, Rh/C, Pt-Rh/C, Pt-SnO$_2$/C and Pt-Rh-SnO$_2$/C. The usual features of the so-called hydrogen and oxygen regions of Pt-based electrodes can be observed [53,54]. On the one hand, the oxide region on Rh- and Sn-based electrocatalysts, $i.e.$ on Rh/C, Pt-Rh/C, Pt-SnO$_2$/C and Pt-Rh-SnO$_2$/C, starts at much lower potentials than on Pt/C ($E = 0.8$ V $vs.$ RHE). The lower onset potential for the former electrocatalysts versus Pt/C may be ascribed to rhodium and tin oxophilic character [55–57]. Electronic interactions between Pt and the non-noble metals may also modify its electronic structure and, as a consequence, favour its affinity toward water dissociation [58]. The oxide reduction also starts at lower potentials on Rh- and Sn-based electrocatalysts showing the higher oxides stability on the electrocatalysts. On the other hand, the hydrogen starts adsorbing at lower potentials on Pt-Rh-based bi- and tri-metallic electrocatalysts than on Pt/C
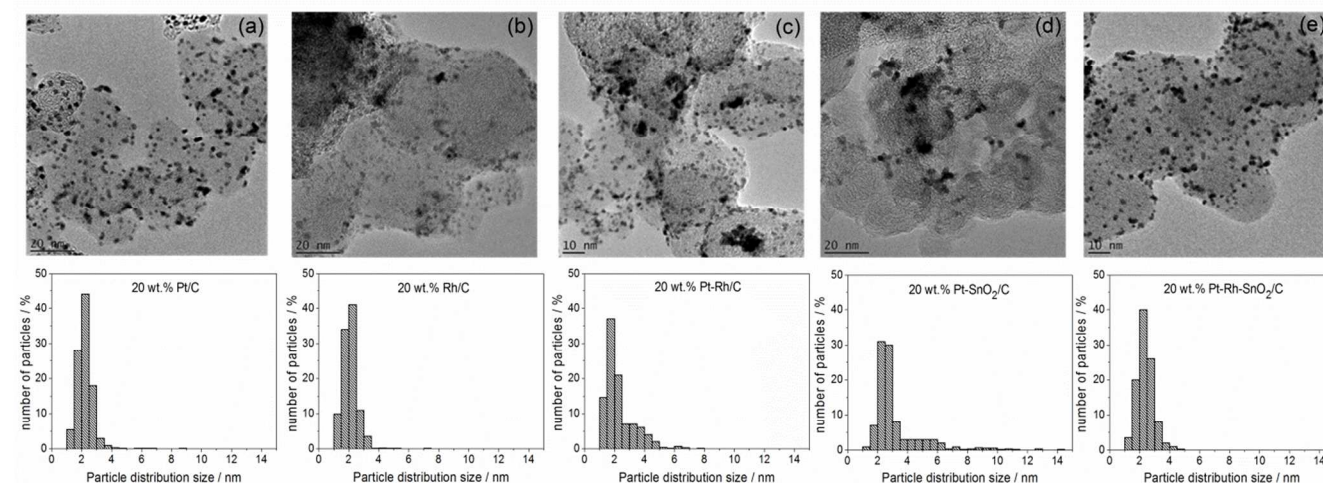

Fig.3 Typical TEM images at (a) 200 000 magnification and associated particle size distribution of the (a) Pt/C, (b) Rh/C, (c) Pt-Rh/C, (d) Pt-SnO$_2$/C and (e) Pt-Rh-SnO$_2$/C electrocatalysts.

ARTICLE TYPE
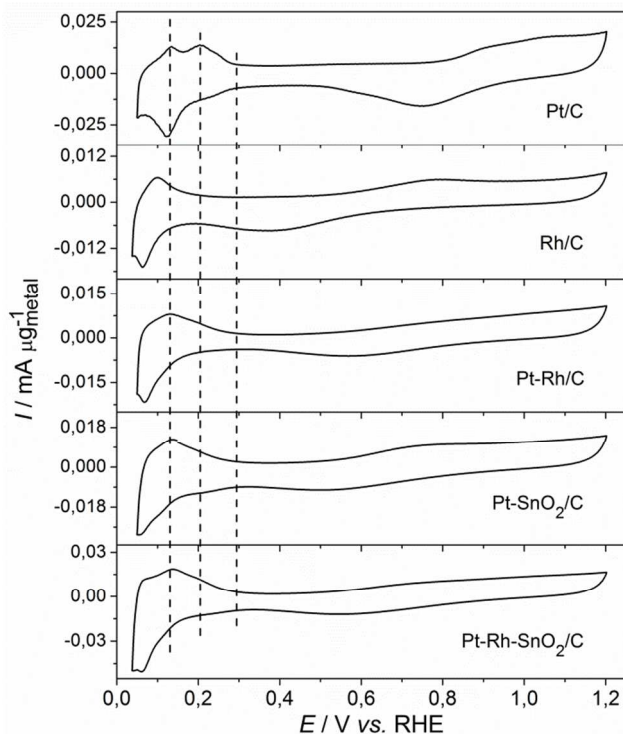
Fig.4 CV in 0.5 M H_2SO_4 on Pt/C, Rh/C, Pt-Rh/C, Pt-SnO$_2$/C and Pt-Rh-SnO$_2$/C electrocatalysts; v = 10 mV s^{-1}; T = 25 °C.
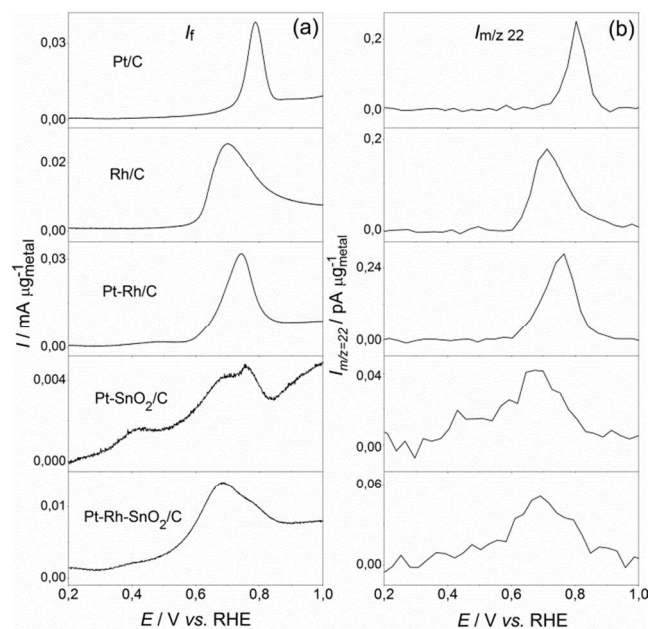

Fig.5 (a) CO-stripping CV in 0.5 M H_2SO_4 in and (b) corresponding MSCV
30 for mass-to-charge ratio m/z 22 on Pt/C, Rh/C, Pt-Rh/C, Pt-SnO2/C and Pt-Rh-SnO$_2$/C; v = 10 mV s^{-1}; T = 25 °C.

5 (E = 0.06 V *vs*. RHE). As it can be seen in Fig. 4, this phenomenon can be attributed to hydrogen lower adsorption potential on Rh/C (E = 0.03 V *vs*. RHE). Likewise, it can be seen that the oxidation peak corresponding to adsorbed hydrogen oxidation on Pt/C is located at *ca*. E = 0.2 V *vs*. RHE versus E =
10 0.12 V *vs*. RHE on Pt-Rh/C, Pt-SnO$_2$/C and Pt-Rh-SnO$_2$/C. On Rh/C, the surface dehydrogenation even operates at E = 0.09 V *vs*. RHE. In other words, H-adsorbates seem less stable at Rh-or/and Sn-containing surfaces than of Pt surfaces. Other results or discussions on Pt surfaces easier dehydrogenation when
15 associated to Rh or Sn can be found in the literature [25,59].

CO stripping

Fig. 5a displays CO-stripping voltammograms recorded on Pt/C, Rh/C, Pt-Rh/C, Pt-SnO$_2$/C and Pt-Rh-SnO$_2$/C, and Fig. 5b the corresponding MSCVs for the mass-to-charge ratio m/z 22. A
20 first comparison between Pt/C and Rh/C shows that the CO-stripping (CO_2 formation) initiates at lower potentials on the latter than on the former: the supply in OH adsorbates on Rh/C at lower potential than on Pt/C (see Fig. 4) may ease CO_{ad} oxidation into CO_2.
25 The electrooxidation of CO adsorbates on Rh/C (E = 0.56 V *vs*. RHE), Pt-Rh/C (E = 0.58 V *vs*. RHE), Pt-SnO$_2$/C (E = 0.25 V *vs*. RHE) and Pt-Rh-SnO$_2$/C (E = 0.30 V *vs*. RHE) initiates at

lower potentials than on Pt/C (E = 0.65 V *vs*. RHE). These values correspond well with the MSCVs illustrating the CO_2 formation efficient at low potential) supply in OH$_{ad}$ species that helps the
35 oxidation of adsorbed CO (bi-functional mechanism, often mentioned for CO and methanol oxidation reactions [60]). Besides, their presence possibly induces a ligand effect operated on Pt electronic structure. This is in agreement with the fact that water dissociation into adsorbed OH-species starts at lower potentials
40 on Pt-Rh-SnO$_2$/C and Pt-Rh/C than on Pt/C. Besides, alloying Rh and Sn with Pt presumably leads to a down-shift of the Pt 5d-band centre caused by the interactions in the lattice between Pt and Rh atoms [61]. This phenomenon would result in a weaker adsorption of CO on Pt atoms of the alloy and thus in the
45 acceleration of the kinetics on Pt-Rh/C.

Potentiodynamic ethanol oxidation reaction

On Pt/C

Fig. 6 presents a comparative study of the first scan of the potentiodynamic voltammetries obtained after a CA at E_{ad} = 0.05,
50 0.3 and 1 V *vs*. RHE. Apparent faster EOR kinetics can be observed during the CV recorded after the CA at E_{ad} = 1 V *vs*. RHE compared to the CV run after the CA at E_{ad} = 0.05 V *vs*. RHE. Also, the associated ionic signals m/z 29 (Fig. 6b), m/z 22 (Fig. 6c) and m/z 61 (Fig. 6d) present a shift toward negative
55 potentials after the CA at E_{ad} = 1 V *vs*. RHE. Clearly, the OH$_{ad}$-species adsorption during the chronoamperometry at E_{ad} = 1 V *vs*. RHE enhanced ethanol oxidation to acetaldehyde at lower potentials. On the contrary, H-adsorbates formed at E_{ad} = 0.05 V *vs*. RHE do inhibit the reaction. Similarly, CO_2 (Fig. 6c) and
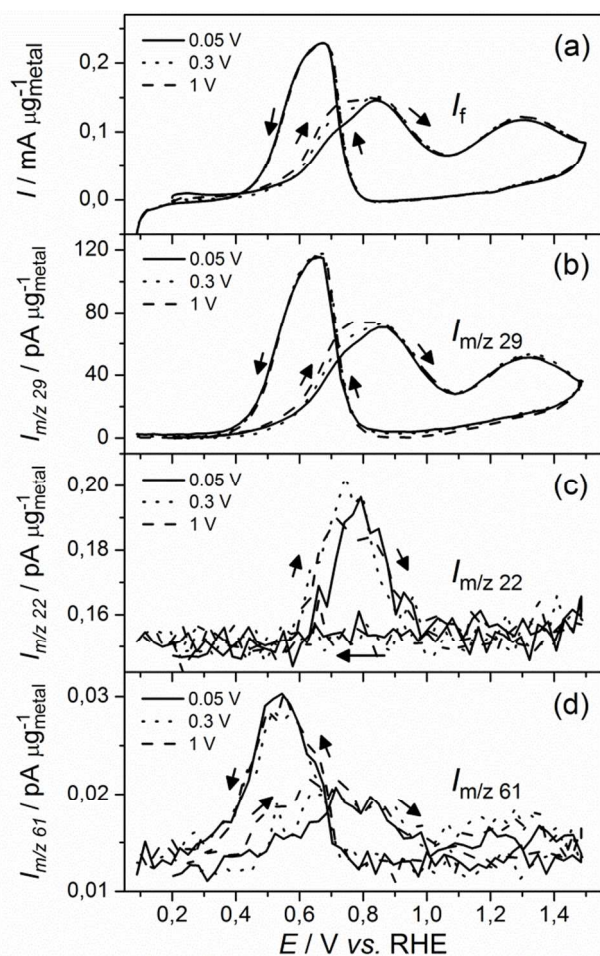
Fig.6 (a) CV of the EOR in 0.5 M H_2SO_4 + 0.1 M EtOH after adsorption at E_{ad} = 0.05 (solid), 1 (dash) and 0.3 V *vs.* RHE (dots) and corresponding MSCV for mass-to-charge ratio (b) *m/z* 29, (c) *m/z* 22 and (d) *m/z* 61 on Pt/C; v = 10 mV s^{-1}; T = 25 °C.

Fig.7 (solid) First and (dash) second scan of the potentiodynamic EOR in 0.5 M H_2SO_4 + 0.1 M EtOH after adsorption at E_{ad} = (a) 0.05 and (b) 1 V *vs.* RHE and corresponding MSCV for mass-to-charge ratio *m/z* 29, *m/z* 22 and *m/z* 61 on Pt/C; v = 10 mV s^{-1}; T = 25 °C.

acetic acid (Fig. 6d) production are also shifted negatively with the presence of OH-adsorbates. Moreover, it seems that ethanol complete electrooxidation into CO_2 is slightly hindered and that the mechanism leading to acetic acid as end-product is favoured. The result is not surprising as the OH_{ad} species required for the EOR and in particular for acetic acid production are provided during the CA at E_{ad} = 1 V *vs.* RHE; in that sense the electrode pre-oxidation facilitates acetic acid formation at lower potentials. These results are in agreement with the literature, as it was demonstrated that Pt-SnO$_2$/C electrocatalysts do not favour ethanol complete oxidation into CO_2, although tin oxide brings hydroxide species at the electrocatalyst surface at lower potentials [8,44,45]. Interestingly, it can also be seen that the acetic acid formation starts at potentials as low as the acetaldehyde production which could signify that adsorbed acetaldehyde is not required as reaction intermediate to generate acetic acid as it is proposed in the literature [4,62]. Finally, the backward scans are in all cases superposed, demonstrating that the pre-formation of such adsorbates cannot maintain durable EOR performance alteration. In all cases, the behaviour monitored at E_{ad} = 0.3 V *vs.* RHE is intermediate between the other two, suggesting that H$_{ad}$-species do inhibit the EOR whereas OH$_{ad}$-species do favour the reaction.
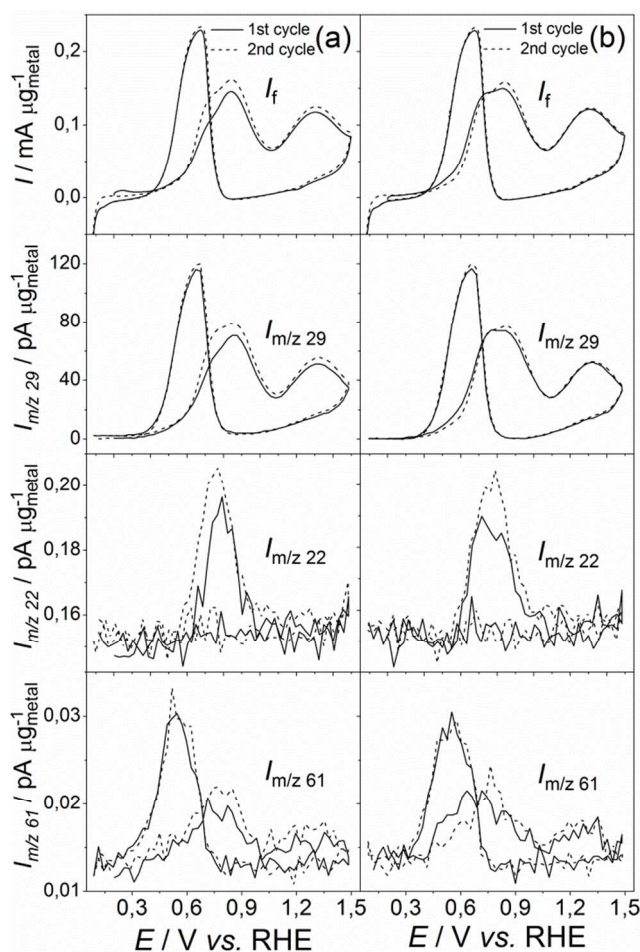
This observation is further confirmed in Fig. 7 which displays the two first cycles of a representative potentiodynamic ethanol electrooxidation on Pt/C and their associated mass-to-charge signals *m/z* 29, *m/z* 22 and *m/z* 61 obtained after a chronoamperometry at E_{ad} = 0.05 (Fig. 7a) and 1 V *vs.* RHE (Fig. 7b). Although ethanol electrooxidation initiates at the same potential (*ca.* E = 0.4 V *vs.* RHE) during the first and second scan, the ethanol oxidation reaction kinetics during the first positive scan is faster than during the following one (Fig. 7b), after OH-species adsorption during the CA at E_{ad} = 1 V *vs.* RHE in 0.5 M H_2SO_4. On the contrary, the hydrogen adsorption during the chronoamperometry at E_{ad} = 0.05 V *vs.* RHE seems to hinder ethanol electrooxidation kinetics, as the first scan is delayed compared to the second one (Fig. 7a). According to the literature [22,25,41], the presence of adsorbed hydrogen hinders ethanol adsorption on the electrocatalyst surface, thereby explaining the slower reaction rate during the first scan of the cyclic voltammetry in Fig. 7a. On the opposite, OH$_{ad}$ could enhance the adsorption/oxidation of organic molecules [63].

On Rh/C

Fig. 8 compares cyclic voltammetries in 0.5 M H_2SO_4 + 0.1 M EtOH on Rh/C preceded by chronoamperometries carried out at E_{ad} = 0.05, 0.3 and 1 V *vs.* RHE. The EOR activity is intensified
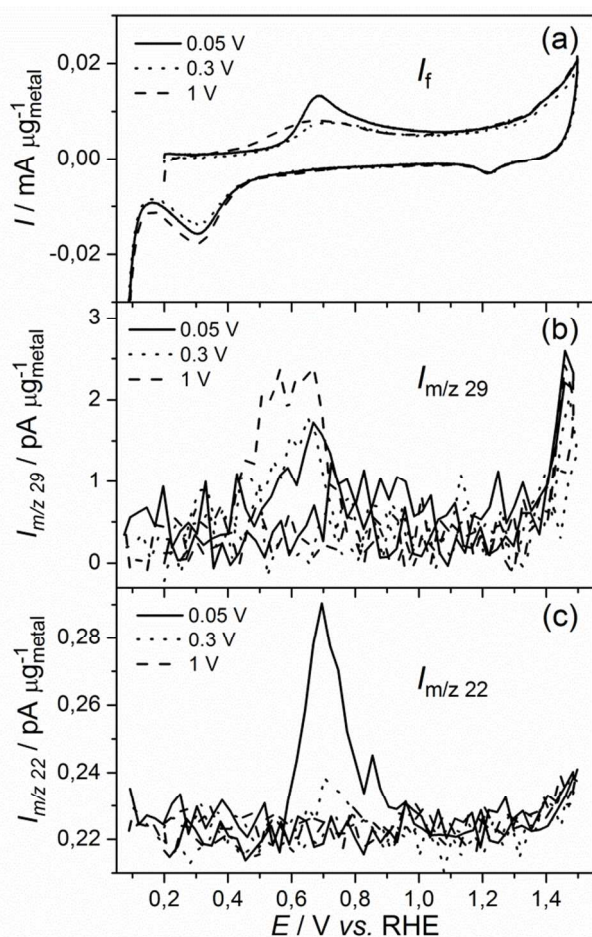
Fig.8 CV of the EOR in 0.5 M H_2SO_4 + 0.1 M EtOH after adsorption at E_{ad} = 0.05 (solid), 1 (dash) and 0.3 V *vs.* RHE (dots) and corresponding MSCV for mass-to-charge ratio (b) *m/z* 29, (c) *m/z* 22 on Rh/C; *v* = 10 mV s^{-1}; *T* = 25 °C.

Fig.9 (solid) First and (dash) second scan of the (a) potentiodynamic EOR in 0.5 M H_2SO_4 + 0.1 M EtOH after adsorption at E_{ad} = 0.05 V *vs.* RHE and corresponding MSCV for mass-to-charge ratio (b) *m/z* 22 and (c) *m/z* 29 on Rh/C; *v* = 10 mV s^{-1}; *T* = 25 °C.

after hydrogen adsorption on the electrocatalyst surface (seen for E_{ad} = 0.05 V *vs.* RHE), although it remains very low in comparison to Pt/C. The EOR CVs for the two other adsorption potential values are inhibited by OH adsorption, OH_{ad} being very stable on rhodium surface (the OH reduction peak is located at *ca.* E = 0.33 V *vs.* RHE *versus* E = 0.75 V *vs.* RHE on Pt/C – see Fig. 4) [64,65]. This observation is confirmed by the weak signals reported after E_{ad} = 0.3 and 1 V *vs.* RHE for the mass-to-charge signal *m/z* 29 and *m/z* 22 in Fig. 8b and Fig. 8c respectively. It can be noticed from the CV preceded by the CA at E_{ad} = 1 V *vs.* RHE that, although rhodium provides OH-species at low potentials, the EOR insignificantly proceeds to the generation of acetaldehyde (*m/z* 29) and CO_2 (*m/z* 22) and does not yield to acetic acid (*m/z* 61 - not shown here). This behaviour is contradictory with that of Pt/C. One assumption could be that ethanol can hardly displace OH-adsorbates on Rh/C surfaces (similarly to sulphate adsorbates [64,66]), conversely to what occurs on Pt/C and, as a consequence, cannot benefit from the electrocatalyst surface composition *a priori* favourable to acetic acid formation. Moreover, ethanol dissociative adsorption leading to CO_2 formation requires free electrocatalytic sites, which is, in our set of experiments, only encountered after the chronoamperometry carried out at E_{ad} = 0.05 V *vs.* RHE (surface
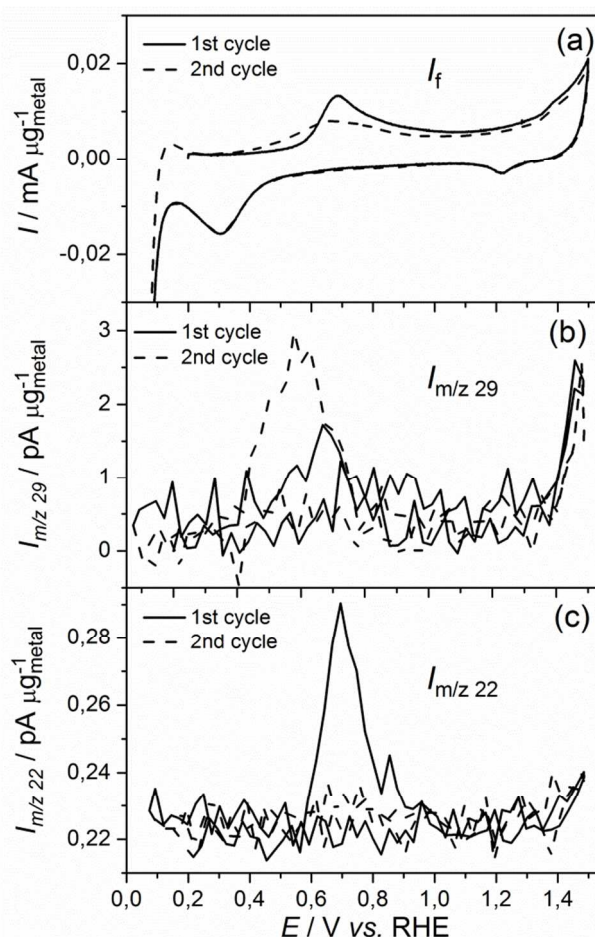
pre-reduction).

Further information can be obtained in Fig. 9 by comparing the first and second cycle of the potentiodynamic ethanol oxidation reaction on Rh/C preceded by hydrogen adsorption at E_{ad} = 0.05 V *vs.* RHE. As shown in Fig. 9a, the second cycle is very similar to the CV obtained after adsorption at E_{ad} = 1 V *vs.* RHE (shown in Fig. 8a). In Fig. 9b, the mass-to-charge signal *m/z* 22 discloses a high CO_2 production (starting at *ca.* E = 0.56 V *vs.* RHE) during the first cycle compared to the second one where almost no CO_2 was detected.

The mass-to-charge signal *m/z* 29 gives further information on the mechanism that operates during the two cycles. During the first cycle, quasi no acetaldehyde is detected (Fig. 9c) while, during the second one, a small but noticeable amount of acetaldehyde emerged during the cyclic voltammetry. Regarding these results, it seems that, during the first cycle, the EOR proceeds almost solely through its complete oxidation pathway leading to CO_2 formation and produces neither acetaldehyde nor acetic acid. On the contrary, a small amount of acetaldehyde and near-zero CO_2 were to be detected during the second scan, similarly to the first scan of the CVs preceded by a chronoamperometry at E_{ad} = 0.3 and 1 V *vs.* RHE (Fig. 8). It can therefore be assumed that the presence of OH adsorbates on the
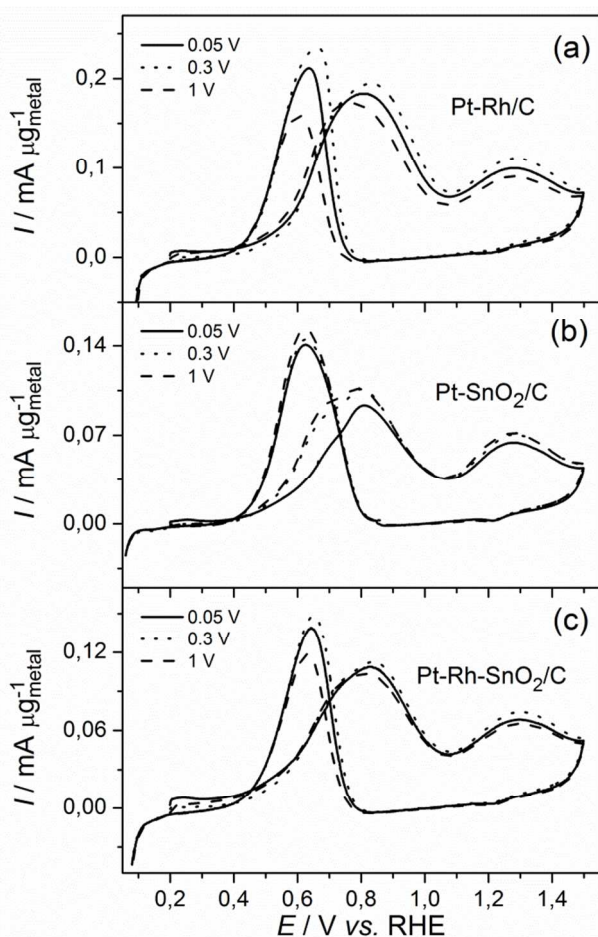
Fig.10 CV of the EOR in 0.5 M H_2SO_4 + 0.1 M EtOH after adsorption at E_{ad} = 0.05 (solid), 1 (dash) and 0.3 V *vs.* RHE (dots) on (a) Pt-Rh/C, (b) Pt-SnO$_2$/C and (c) Pt-Rh-SnO$_2$/C; v = 10 mV s^{-1}; T = 25 °C.

5 Rh/C surface inhibits considerably the complete EOR leading to CO_2 (by impeding ethanol adsorption) and even slightly encourages acetaldehyde formation (ethanol dissociative adsorption is no longer possible due to the overwhelming OH-adsorbates on rhodium surface). Finally, a large rise of the signal
10 m/z 29 is observed at high potentials (E > 1.2 V *vs.* RHE, Fig. 9c) which can only correspond to acetaldehyde formation (a similar increase was obtained with signal m/z 15 ([CH_3^+]) not shown here). This acetaldehyde formation is expected to come from the oxidation of C_2-species that only oxidize at high potentials [24,67].

15 **On Pt based bi- and tri-metallic electrocatalysts**

In Fig. 10, a particular attention is paid to the influence of the different chronoamperometries achieved prior to the cyclic voltammetries in 0.5 M H_2SO_4 + 0.1 M EtOH on Pt-Rh/C, Pt-SnO$_2$/C and Pt-Rh-SnO$_2$/C. On Pt-Rh/C, they obviously do not
20 impact much the reaction initiation (Fig. 10a). As platinum and rhodium have opposite behaviours regarding the strength of H- and OH-adsorbates, the lack of adsorbate effect could be imputed to a combined effect of Pt and Rh metals lowering the stability of OH$_{ad}$ and H$_{ad}$ on Pt-Rh/C and thus easing their displacement by
25 ethanol molecules. Similarly, the EOR on Pt-Rh-SnO$_2$/C (Fig. 10c) does not seem much influenced by the adsorbates. However, as for Pt/C, the EOR kinetics on Pt-SnO$_2$/C (Fig. 10b) is hindered by hydrogen adsorbates. This is an indirect evidence that tin
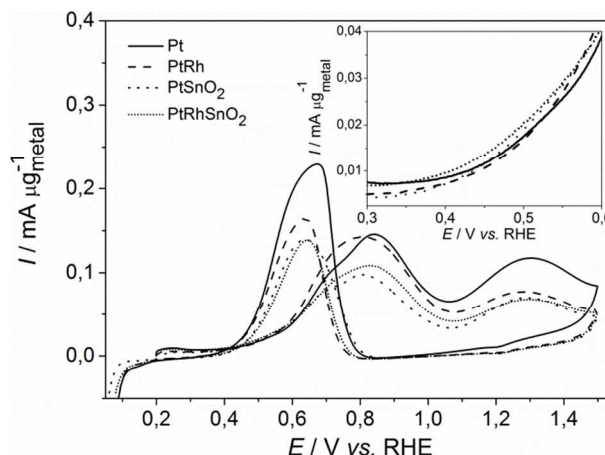

30 **Fig. 11** (a) CV of the EOR in 0.5 M H_2SO_4 + 0.1 M EtOH after CA at E_{ad} = 0.05 V *vs.* RHE on Pt/C (solid), Pt-Rh/C (dash), Pt-SnO$_2$/C (dots) and Pt-Rh-SnO$_2$/C (short dots); v = 10 mV s^{-1}; T = 25 °C.

oxide does not help the surface dehydrogenation, and that such composite electrocatalyst likely operates through a bifunctional
35 mechanism: Pt adsorbs ethanol and dehydrogenates it, whereas SnO$_2$ "only" provides OH$_{ad}$ species (at lower potential than Pt).

During the negative scan, the initiation of the ethanol electrooxidation on Pt-Rh/C and Pt-Rh-SnO$_2$/C occurs at a lower potential and at a lower extent after the CA at E_{ad} = 1 V *vs.* RHE
40 compared to the CVs obtained after E_{ad} = 0.05 and 0.3 V *vs.* RHE. This phenomenon is attributed to the higher stability of the hydroxide adsorbates which reduce on rhodium at a lower potential than on platinum (see Fig. 4) and which prevent ethanol from adsorbing/oxidizing on the rhodium surface. On the
45 contrary, the EOR on Pt-SnO$_2$/C remains unchanged, even though hydroxide adsorbates are more stable on tin oxide. This is interpreted by the fact that ethanol does not adsorb on SnO$_2$, the role of which is only to provide OH$_{ad}$-species at lower potential.

EOR comparative study between the electrocatalysts

50 Fig. 11 compares the EOR after a chronoamperometry at E_{ad} = 0.05 V *vs.* RHE on Pt/C, Pt-Rh/C, Pt-SnO$_2$/C and Pt-Rh-SnO$_2$/C. The ethanol electrooxidation on Rh/C was ignored as the reaction electroactivity was too low in comparison to the other electrocatalysts. As shown in the inset of Fig. 11, the EOR
55 initiates on all electrocatalysts at *ca.* E = 0.35 V *vs.* RHE. Nonetheless, a higher reaction electroactivity (normalized by the total metal mass) was recorded on Pt-Rh-SnO$_2$/C and on Pt-SnO$_2$/C compared to Pt/C until E = 0.62 V *vs.* RHE. A faster current increase during the EOR at very low potential values can
60 be explained by faster ethanol dehydrogenation kinetics (2e$^-$) or by an enhanced ethanol electrooxidation toward acetic acid (4e$^-$) or CO_2 (12 e$^-$).

Conversely, Pt/C clearly surpasses all the multi-metallic electrocatalysts at E > 0.62 V *vs.* RHE. Pt lower metal content in
65 Pt-SnO$_2$/C (see Table 1) and Pt-Rh-SnO$_2$/C compared to Pt/C (which is the most electroactive pure metal in acid medium) could explain the larger peak current at E = 0.88 V *vs.* RHE on the latter (the current is normalized to the total mass of metal). However, this explanation does not work for Pt-Rh/C, the Pt:Rh
70 ratio of which is almost 1:1. Although the EOR activity is not very large on Rh alone (Fig. 8) compared to Pt (Fig. 6), the EOR on Pt-Rh/C exhibits currents as high as on Pt/C. This could be
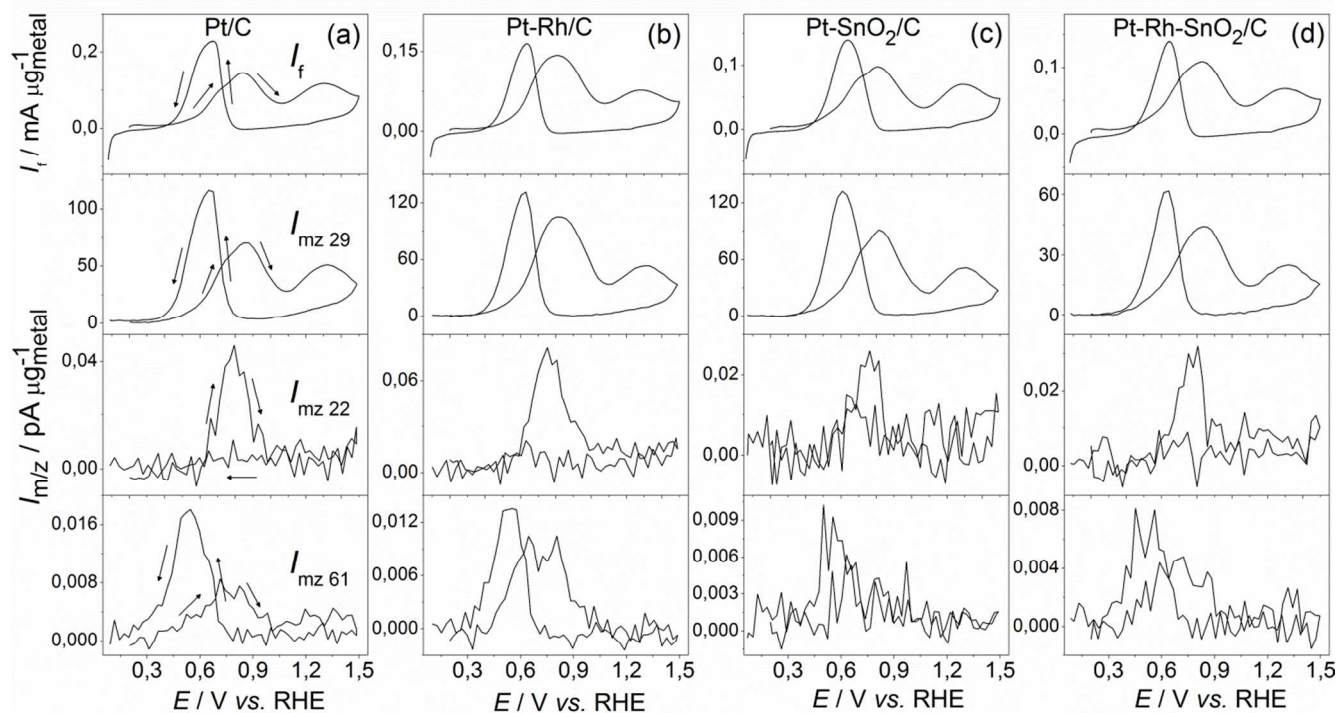
ARTICLE TYPE

Fig.12 CV of the EOR in 0.5 M H_2SO_4 + 0.1 M EtOH after adsorption at E_{ad} = 0.05 on (a) Pt/C, (b) Pt-Rh/C, (c) Pt-SnO$_2$/C and (d) Pt-Rh-SnO$_2$/C and corresponding MSCV for mass-to-charge ratio m/z 29, m/z 22 and m/z 61; v = 10 mV s^{-1}; T = 25 °C.

due to an alloy effect between the two metals and to a facilitation of the C-C bound breaking in the presence of Rh.

Regarding the mass-to-charge signals m/z 22, m/z 29 and m/z 61 (Fig. 12), acetaldehyde formation (m/z 29) starts at *ca.* E = 0.27 V *vs.* RHE on Pt-Rh/C and E = 0.24 V *vs.* RHE on Pt-SnO$_2$/C and Pt-Rh-SnO$_2$/C versus E = 0.31 V *vs.* RHE on Pt/C. This observation agrees with the higher dehydrogenation on Pt-Rh/C, Pt-SnO$_2$/C and Pt-Rh-SnO$_2$/C highlighted in Fig. 4. These values are slightly lower than those depicting the faraday current onset, due to the non-quantitative formation of acetaldehyde generating a too low current to be observable in Fig. 11. Acetic acid formation starts shortly after *ca.* E = 0.35 V *vs.* RHE on Pt-Rh-SnO$_2$/C and E = 0.32 V *vs.* RHE on Pt-Rh/C and Pt/C. Pt-SnO$_2$/C seems to ease acetic acid formation better than the other electrocatalysts at low potential (onset at *ca.* E = 0.28 V *vs.* RHE), because the SnO$_2$ moiety is capable to easily provide OH$_{ad}$-species to the acetaldehyde adsorbed at the Pt moiety. However, at higher potential, acetic acid formation seems more enhanced on Pt-Rh/C electrocatalyst. Conversely to the literature [8,45], our synthesized Pt-SnO$_2$/C electrocatalyst does not seem to favour the pathway leading to acetic acid formation compared to Pt/C. PtSnO$_2$/C peculiar physical structure (presence of larger nanoparticles and agglomerates) could explain these divergent results. Unfortunately, the few existing studies focused on the nanoparticles size effect [18,41] do not give evidence of an influence of the nanoparticles size on the EOR pathway. Finally, CO$_2$

generation seems slightly shifted on Pt-based bi- and tri-metallic electrocatalysts compared to Pt/C. Indeed, CO$_2$ could be detected at potentials as low as E = 0.54 V *vs.* RHE on Pt-Rh-SnO$_2$/C versus E = 0.58 V *vs.* RHE on Pt-Rh/C and E = 0.61 V *vs.* RHE on Pt/C. CO$_2$ was also generated during the negative scan on Pt-SnO$_2$/C. Ionic (m/z 22, m/z 29 and m/z 61) current onsets of all studied electrocatalysts (comprised Rh/C) are summarized in Table 2.

CO$_2$ current efficiency

The CO$_2$ current efficiency (CCE) was determined from potendiodynamic voltammetries and the corresponding mass-to-charge signal m/z 22 between E = 0.5 and 0.9 V *vs.* RHE (0.1 V step) on Pt/C, Pt-Rh/C, Pt-SnO$_2$/C and Pt-Rh-SnO$_2$/C. Regarding the previous results of Fig. 12, the chronoamperometries at E_{ad} = 0.05, 0.3 and 1 V *vs.* RHE do impact the EOR and more specifically the CO$_2$ production. Consequently, the CCE variation versus the potential was evaluated after chronoamperometries at E_{ad} = 0.05, 0.3 and 1 V *vs.* RHE.

It can be noticed in Fig. 13 that the CCE evolution can be separated in two steps for all electrocatalysts: a first ascending phase between E = 0.5 and *ca.* 0.7 - 0.8 V *vs.* RHE (depending on the previous CA), where the CCE increases against the potential; a second one at E > 0.7 - 0.8 V *vs.* RHE where the CCE shrinks. The CCE rise in the first potential region can reasonably be explained by OH growing adsorption permitting the oxidation of

Table 2 Onset potential values of the mass-to-charge signals m/z 22, m/z 29 and m/z 61 measured on Pt/C, Rh/C, Pt-Rh/C, Pt-SnO$_2$/C and Pt-Rh-SnO$_2$/C during the potentiodynamic EOR recorded after a CA at E_{ad} = 0.05 V $vs.$ RHE.

m/z	Pt/C	Rh/C	Pt-Rh/C	Pt-SnO$_2$/C	Pt-Rh-SnO$_2$/C
			E / V $vs.$ RHE		
29	0.31	0.27	0.27	0.24	0.24
22	0.61	0.56	0.58	0.59	0.54
61	0.35	-	0.33	0.28	0.35

adsorbed CO. A second reason could be the improved C-C bond breaking ability gained by the electrocatalyst with the potential increase (although previous studies reported ethanol dissociative adsorption at potentials as low as E = 0.05 V $vs.$ RHE [24,67]). On the contrary, in the second potential region (E > 0.7 - 0.8 V $vs.$ RHE), CO$_2$ generation is more and more hindered as the potential increases. It is believed that above a certain potential, the presence of adsorbates on the electrocatalyst surface prevents ethanol dissociative adsorption and *a fortiori* CO$_2$ generation. These adsorbates are supposedly OH$_{ad}$ and ethanol intermediates [16,68] and are believed to sterically impede the ethanol dissociative adsorption. Fig. 13c shows the relative lower CCE values obtained when the potentiodynamic voltammetry is preceded by the CA at E_{ad} = 1 V $vs.$ RHE in comparison to the CVs preceded by the CA at E_{ad} = 0.05 and 0.3 V $vs.$ RHE. It is supposed that adsorbed hydroxide species did not have time to desorb completely from the electrocatalyst surface at the beginning of the CV and that the remaining OH$_{ad}$-species hinder ethanol dissociative adsorption and thus CO$_2$ generation. An accumulation of ethanol adsorbates on the electrocatalyst surface could also prevent ethanol dissociative adsorption (which likely requires more than two free neighbouring electrocatalytic sites). This explanation is supported by the oxidation of CH$_x$- and C$_2$-adsorbates only at potentials as high as E = 0.9 V $vs.$ RHE [67]. Identifying these ethanol adsorbates would require a thorough IR analysis and is beyond the scope of this study.

Among the studied electrocatalysts, Pt-Rh-SnO$_2$/C demonstrates the highest CO$_2$ current efficiency in all three protocols while Pt/C and Pt-SnO$_2$/C displayed the lowest values. A higher CO$_2$ generation on Pt-Rh-SnO$_2$/C than on PtSnO$_2$/C evaluated by infrared techniques is also reported in the literature [47]. Low CCE values on Pt/C and Pt-SnO$_2$/C are also supported in the literature in other DEMS studies [8,44]. According to the authors, the larger CCE values obtained on Rh-containing electrocatalysts (Pt-Rh/C and Pt-Rh-SnO$_2$/C) are attributed to the stronger adsorption of the ethanol adsorbates on the electrocatalyst surface which enhances the C-C bond cleavage. On Pt/C, the strength of the bond is believed to be too weak which results into two negative consequences for the complete EOR: the desorption of the ethanol adsorbates (more precisely the acetyl ones, as proposed by Iwasita and Pastor [16]) soon after ethanol dehydrogenation, which leads to the production of acetaldehyde or acetic acid; the slower kinetics of the C-C bond cleavage compared to rhodium. The larger CCE values on Pt-Rh-SnO$_2$/C compared to Pt-Rh/C are attributed both to the OH-supply at low potential via SnO$_2$ and to the freeing of the rhodium sites from hydroxide adsorbates by the same tin oxide.

The influence of the chronoamperometries at E_{ad} = 0.05, 0.3 and 1 V $vs.$ RHE in 0.5 M H$_2$SO$_4$ run before the potentiodynamic voltammetries on the CO$_2$ current efficiency is compared in Fig.
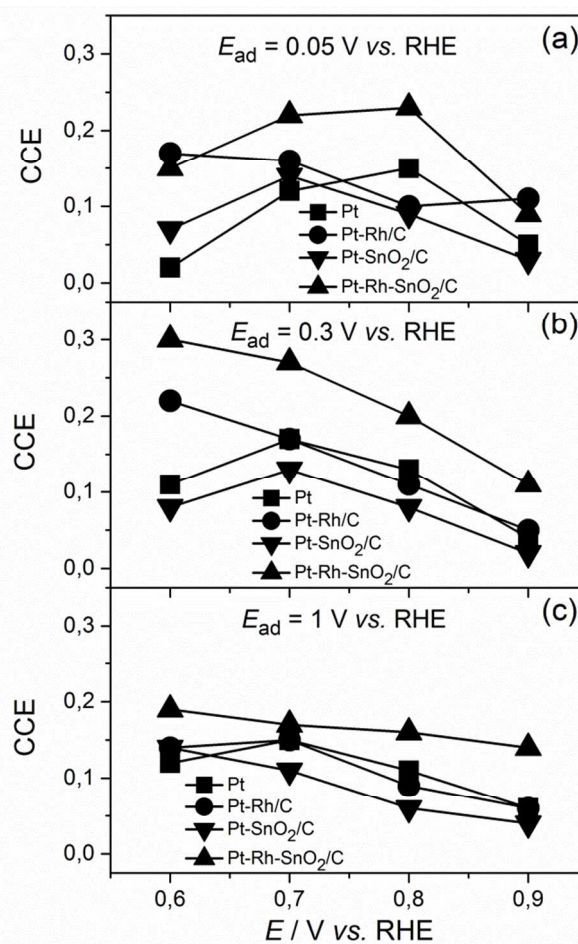

Fig.13 Potentiodynamic EOR CO$_2$ current efficiency (CCE) values deduced from cyclic voltammetries in 0.5 M H$_2$SO$_4$ + 0.1 M EtOH on Pt/C, Pt-Rh/C, Pt-SnO$_2$/C and Pt-Rh-SnO$_2$/C preceded by CA at E_{ad} = (a) 0.05, (b) 0.3 and (c) 1 V $vs.$ RHE.

13a, Fig. 13b and Fig. 13c respectively. For each Pt-based electrocatalysts, the CCE values are generally lower after the chronoamperometry at E_{ad} = 1 V $vs.$ RHE illustrating the observation done with Fig. 12. Although adsorbed OH-species are necessary to oxidize CO$_{ad}$, a large coverage of the electrocatalyst surface by the OH-adsorbates may hinder CO$_{ad}$ formation coming from adsorbed acetaldehyde or direct ethanol dissociative adsorption. The CA at E_{ad} = 0.3 V $vs.$ RHE seems to enhance CO$_2$ production during the following cyclic voltammetry. Although the original goal of this chronoamperometry was to start the cyclic voltammetry without any adsorbates at the electrocatalyst surface, the mandatory change of solution during the last four minutes of the CA may have, on the contrary, provoked ethanol dissociative adsorption into CO$_{ad}$ before the beginning of the CV. These CO$_{ad}$-species then likely oxidized as soon as hydroxide molecules started adsorbing on the electrocatalyst surface. That could explain the higher CCE values in Fig. 13b and also why CO$_2$ generation starts at potentials as low as E = 0.5 V $vs.$ RHE on Pt-Rh-SnO$_2$/C, which also corresponds to the beginning of OH$_{ad}$ formation on the tri-metallic electrocatalyst (see Fig. 4).
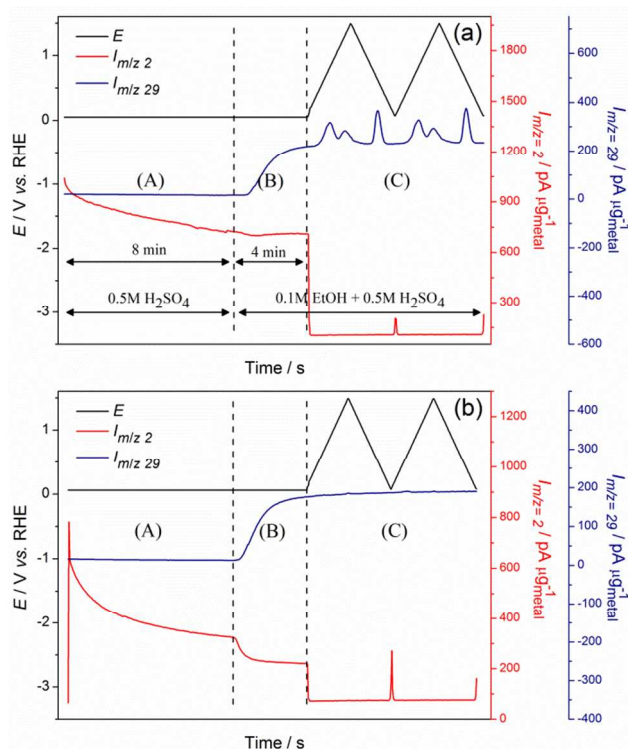
Zoom on the CA at E_{ad} = 0.05 V $vs.$ RHE

Fig.14 Evolution of the potential and mass-to-charge ratio signals *m/z* 2 and *m/z* 29 *vs.* time on (a) Pt/C and (b) Rh/C during three consecutive steps: (A) hydrogen adsorption in 0.5 M H_2SO_4 at E_{ad} = 0.05 V *vs.* RHE, (B) the solution change in 0.5 M H_2SO_4 + 0.1 M EtOH and (C) the potentiodynamic ethanol oxidation reaction starting at E = 0.2 V *vs.* RHE.

The aim of this section is to demonstrate the difficulty for ethanol to displace adsorbed hydrogen species on Pt/C conversely to Rh/C. To that purpose, the presented figures show the evolution of the potential (left y-axis) and of the mass-to-charge signals (right y-axis) *m/z* 29 ([CHO^+]) and *m/z* 2 ([H_2^+]) against the time during the chronoamperometry carried out at E_{ad} = 0.05 V *vs.* RHE, followed by the voltamperogram in 0.5 M H_2SO_4 + 0.1 M EtOH (similarly to Fig. 1, but with the additional evolution of the MSCVs *m/z* 2 and *m/z* 29). The particularly interesting information here relies in the behaviour of the signal *m/z* 2 after the solution switch from 0.5 M H_2SO_4 to 0.5 M H_2SO_4 + 0.1 M EtOH after the first eight minutes of the CA. The mass-to-charge signal *m/z* 29 is used to evidence the solution switch (to a solution containing ethanol) after the first eight minutes of CA. As observed in Fig. 14a and Fig. 14b, the appearance of this signal is slightly delayed (which explains the non-superposition of the vertical dashed line with the signal *m/z* 29). This delay corresponds to the time required by the solution to flow in the capillaries, reach the electrochemical cell and be pumped inside the mass spectrometer.

First and foremost, the first decrease of the mass-to-charge signal *m/z* 2 during the first eight minutes of the CA corresponds to a "normal" hydrogen generation response to the potential step from E_{ad} = 1 to 0.05 V *vs.* RHE (a first CA not shown in Fig. 14 was carried out at E_{ad} = 1 V *vs.* RHE in 0.5 M H_2SO_4 during 30 s to clean the electrocatalyst surface from potentially residual ethanol adsorbates coming from a previous CV in 0.5 M H_2SO_4 + 0.1 M EtOH). Contrary to the first step of the CA similar on Pt/C and Rh/C, the second step differs significantly on the two

electrocatalysts: on Pt/C (Fig. 14a), the initial drop of the ionic (*m/z* 2) current during the first eight minutes of the CA is followed by its slight rise/stabilization appearing simultaneously to the increase of the signal *m/z* 29 (corresponding here to the progressive presence of 0.1 M ethanol in the electrolyte) and may sign a low formation of H_2 as by-product of the ethanol dehydrogenation. However, this hypothesis cannot be proved with the mass-to-charge signal *m/z* 29, biased by the ethanol concentration variation which prevents from detecting the possible low acetaldehyde formation. As far as the authors are concerned, the high constant ionic (*m/z* 2) current recorded on Pt/C is more believed to illustrate H_2 steady formation and thus ethanol difficulty to adsorb on the electrocatalyst, as evidenced in Fig. 6 and Fig. 7. On the contrary, a further shrinkage of the ionic (*m/z* 2) current is recorded on Rh/C (Fig. 14b). This phenomenon can be explained by the ethanol adsorption taking place quantitatively on the electrocatalyst surface, which blocks rhodium electroactive sites and hinders dramatically the hydrogen generation. This result is in agreement with the larger currents generated during the EOR after the CA at E_{ad} = 0.05 V *vs.* RHE (Fig. 8 and Fig. 9).

Conclusions

The influence of the presence of H- and OH-adsorbates on the potentiodynamic ethanol electrooxidation was studied on home-made Pt/C, Rh/C, Pt-Rh/C, Pt-SnO_2/C and Pt-Rh-SnO_2/C by differential electrochemical mass spectrometry (DEMS) in a flow cell system. Prior to the cyclic voltammetries, a chronoamperometry at E_{ad} = 0.05 and 1 V *vs.* RHE was applied in order to adsorb these adsorbates. For the sake of comparison, another adsorption potential was chosen at E_{ad} = 0.3 V *vs.* RHE in the double layer region. The three main products of the ethanol oxidation reaction (EOR), acetaldehyde, acetic acid and CO_2, were detected using the mass-to-charge signals *m/z* 29, *m/z* 22 and *m/z* 61, respectively.

The physical investigation of the electrocatalysts revealed crystallized round-shaped metal nanoparticles well-dispersed on the carbon support. The presence of some agglomerates and large nanoparticles were however observed by TEM on Pt-Rh/C and to a larger extent on Pt-SnO_2/C.

The comparison of the first and second cycle of the CVs on Pt/C revealed a kinetics slow-down during the first scan following the CA at E_{ad} = 0.05 V *vs.* RHE, whereas a shift toward negative potentials was observed after the CA at E_{ad} = 1 V *vs.* RHE. These results were interpreted by the hindrance of the ethanol adsorption/electrooxidation due to H_{ad} and by an easier replacement of OH-adsorbates by ethanol molecules.
Results on Rh/C were opposite to platinum. The EOR proceeded almost entirely through its complete pathway toward CO_2 after hydrogen adsorption, while the activity was highly lowered during the second scan of the CV preceded by the CA at E_{ad} = 0.05 V *vs.* RHE. A low EOR activity was also reported after the CA at E_{ad} = 0.3 and 1 V *vs.* RHE. The high OH_{ad} stability on Rh/C likely prevents their displacement by bulk ethanol molecules and thus their electrooxidation.

Similarly to Pt/C, the EOR on Pt-SnO_2/C was hindered by H-adsorbates while the EOR on Pt-Rh/C and Pt-Rh-SnO_2/C did not show much influence of the adsorbates. The last result was

explained by Pt and Rh opposite behaviours. The comparison between the electrocatalysts revealed a slightly lower EOR onset potential on Pt-SnO$_2$/C and Pt-Rh-SnO$_2$/C than on Pt/C, which was corresponding to ethanol better dehydrogenation into acetaldehyde. CO$_2$ generation was detected at lower potentials on Pt-Rh-SnO$_2$/C than on the other electrocatalysts. The CO$_2$ currency efficiency (CCE) was finally determined for each electrocatalyst and demonstrated higher values on Pt-Rh-SnO$_2$/C, regardless of the adsorption process preceding the cyclic voltammetries. The last result was explained by a stronger adsorption of the ethanol adsorbates on the rhodium surface than on platinum favouring the C-C bond cleavage.

Finally, The representation *versus* time of the mass-to-charge ratio *m/z* 2 gives further insight on ethanol ability to displace the hydrogen adsorbates: ethanol is unable to dislodge H$_{ad}$ significantly on Pt/C (but may partially dehydrogenize and form H$_2$ as by-product), whereas this operation is successfully performed on Rh/C.

Acknowledgements

Notes

* Corresponding author

a Fraunhofer Institute for Chemical Technology ICT, Joseph-von-Fraunhofer-Straße 7, 76327 Pfinztal, Germany

b Univ. Grenoble Alpes, LEPMI, F-38000 Grenoble, France

c CNRS, LEPMI, F-38000 Grenoble, France

Member of the French University Institute (IUF)

References

1   C. Lamy, S. Rousseau, E. M. Belgsir, C. Coutanceau and J.-M. Léger, *Electrochimica Acta*, 2004, **49**, 3901–3908.

2   M. H. Shao and R. R. Adzic, *Electrochimica Acta*, 2005, **50**, 2415–2422.

3   H. Wang, Z. Jusys and R. J. Behm, *J. Phys. Chem. B*, 2004, **108**, 19413–19424.

4   G. A. Camara and T. Iwasita, *J. Electroanal. Chem.*, 2005, **578**, 315–321.

5   N. Fujiwara, K. A. Friedrich and U. Stimming, *J. Electroanal. Chem.*, 1999, **472**, 120–125.

6   C. Cremers, D. Bayer, J. O. Meier, S. Berenger, B. Kintzel, M. Joos and J. Tübke, *ECS Trans.*, 2010, **25**, 27–37.

7   F. Delime, J.-M. Léger and C. Lamy, *J. Appl. Electrochem.*, 1999, **29**, 1249–1254.

8   H. Wang, Z. Jusys and R. J. Behm, *J. Power Sources*, 2006, **154**, 351–359.

9   S. Rousseau, C. Coutanceau, C. Lamy and J.-M. Léger, *J. Power Sources*, 2006, **158**, 18–24.

10 V. Rao, C. Cremers, U. Stimming, L. Cao, S. Sun, S. Yan, G. Sun and Q. Xin, *J. Electrochem. Soc.*, 2007, **154**, B1138–B1147.

11 J. P. I. de Souza, S. L. Queiroz, K. Bergamaski, E. R. Gonzalez and F. C. Nart, *J. Phys. Chem. B*, 2002, **106**, 9825–9830.

12 J. Willsau and J. Heitbaum, *J. Electroanal. Chem. Interfacial Electrochem.*, 1985, **194**, 27–35.

13 P. Gao, S.-C. Chang, Z. Zhou and M. J. Weaver, *J. Electroanal. Chem. Interfacial Electrochem.*, 1989, **272**, 161–178.

14 L.-W. H. Leung, S.-C. Chang and M. J. Weaver, *J. Electroanal. Chem. Interfacial Electrochem.*, 1989, **266**, 317–336.

15 L.-W. H. Leung, S.-C. Chang and M. J. Weaver, *J. Electroanal. Chem. Interfacial Electrochem.*, 1989, **266**, 317–336.

16 T. Iwasita and E. Pastor, *Electrochimica Acta*, 1994, **39**, 531–537.

17 T. Iwasita, R. Dalbeck, E. Pastor and X. Xia, *Electrochimica Acta*, 1994, **39**, 1817–1823.

18 J. Perez, V. A. Paganin and E. Antolini, *J. Electroanal. Chem.*, 2011, **654**, 108–115.

19 D. Bayer, S. Berenger, M. Joos, C. Cremers and J. Tübke, *Int. J. Hydrog. Energy*, 2010, **35**, 12660–12667.

20 D. Bayer, S. Berenger, C. Cremers and J. Tübke, *ECS Trans.*, 2010, **25**, 95–103.

21 D. A. Cantane, W. F. Ambrosio, M. Chatenet and F. H. B. Lima, *J. Electroanal. Chem.*, 2012, **681**, 56–65.

22 K. Bergamaski, E. R. Gonzalez and F. C. Nart, *Electrochimica Acta*, 2008, **53**, 4396–4406.

23 S. Sun, M. C. Halseid, M. Heinen, Z. Jusys and R. J. Behm, *J. Power Sources*, 2009, **190**, 2–13.

24 H. Wang, Z. Jusys and R. j. Behm, *Fuel Cells*, 2004, **4**, 113–125.

25 K. Bergamaski, J. F. Gomes, B. E. Goi and F. C. Nart, *Eclética Quím.*, 2003, **28**, 87–92.

26 Z. Jusys and R. J. Behm, *J. Phys. Chem. B*, 2001, **105**, 10874–10883.

27 T. Iwasita, F. C. Nart and W. Vielstich, *Berichte Bunsenges. Für Phys. Chem.*, 1990, **94**, 1030–1034.

28 V. M. Schmidt, R. Ianniello, E. Pastor and S. González, *J. Phys. Chem.*, 1996, **100**, 17901–17908.

29 N. Fujiwara, K. A. Friedrich and U. Stimming, *J. Electroanal. Chem.*, 1999, **472**, 120–125.

30 G. A. Camara, R. B. de Lima and T. Iwasita, *Electrochem. Commun.*, 2004, **6**, 812–815.

31 K. Bergamaski, E. R. Gonzalez and F. C. Nart, *Electrochimica Acta*, 2008, **53**, 4396–4406.

32 S. Y. Shen, T. S. Zhao and J. B. Xu, *Int. J. Hydrog. Energy*, 2010, **35**, 12911–12917.

33 F. Colmati, E. Antolini and E. R. Gonzalez, *J. Power Sources*, 2006, **157**, 98–103.

34 A. Kowal, M. Li, M. Shao, K. Sasaki, M. B. Vukmirovic, J. Zhang, N. S. Marinkovic, P. Liu, A. I. Frenkel and R. R. Adzic, *Nat. Mater.*, 2009, **8**, 325–330.

35 M. Li, A. Kowal, K. Sasaki, N. Marinkovic, D. Su, E. Korach, P. Liu and R. R. Adzic, *Electrochimica Acta*, 2010, **55**, 4331–4338.

36 L. ZHAO, S. MITSUSHIMA, A. ISHIHARA, K. MATSUZAWA and K. OTA, *Chin. J. Catal.*, 2011, **32**, 1856–1863.

37 G. García, N. Tsiouvaras, E. Pastor, M. A. Peña, J. L. G. Fierro and M. V. Martínez-Huerta, *Int. J. Hydrog. Energy*, 2012, **37**, 7131–7140.

38 E. Lee, A. Murthy and A. Manthiram, *Electrochimica Acta*, 2011, **56**, 1611–1618.

39 E. Méndez, J. L. Rodríguez, M. C. Arévalo and E. Pastor, *Langmuir*, 2002, **18**, 763–772.

40 N. R. de Tacconi, R. O. Lezna, B. Beden, F. Hahn and C. Lamy, *J. Electroanal. Chem.*, 1994, **379**, 329–337.

41 F. H. B. Lima, D. Profeti, W. H. Lizcano-Valbuena, E. A. Ticianelli and E. R. Gonzalez, *J. Electroanal. Chem.*, 2008, **617**, 121–129.

42 F. H. B. Lima and E. R. Gonzalez, *Electrochimica Acta*, 2008, **53**, 2963–2971.

43 S. Sen Gupta and J. Datta, *J. Electroanal. Chem.*, 2006, **594**, 65–72.

44 L. Jiang, L. Colmenares, Z. Jusys, G. Q. Sun and R. J. Behm, *Electrochimica Acta*, 2007, **53**, 377–389.

45 F. Vigier, C. Coutanceau, F. Hahn, E. M. Belgsir and C. Lamy, *J. Electroanal. Chem.*, 2004, **563**, 81–89.

46 A. V. Tripković, K. D. Popović, J. D. Lović, V. M. Jovanović, S. I. Stevanović, D. V. Tripković and A. Kowal, *Electrochem. Commun.*, 2009, **11**, 1030–1033.

47 M. Li, A. Kowal, K. Sasaki, N. Marinkovic, D. Su, E. Korach, P. Liu and R. R. Adzic, *Electrochimica Acta*, 2010, **55**, 4331–4338.

48 M. Li, W.-P. Zhou, N. S. Marinkovic, K. Sasaki and R. R. Adzic, *Electrochimica Acta*, 2013, **104**, 454–461.

49 F. Colmati, E. Antolini and E. R. Gonzalez, *J. Alloys Compd.*, 2008, **456**, 264–270.

50 J. Wang, S. Wasmus and R. F. Savinell, *J. Electrochem. Soc.*, 1995, **142**, 4218–4224.

51 C. Cremers, D. Bayer, B. Kintzel, M. Joos, F. Jung, M. Krausa and J. Tübke, *ECS Trans.*, 2008, **16**, 1263–1273.

52 H. Baltruschat, *J. Am. Soc. Mass Spectrom.*, 2004, **15**, 1693–1706.

53 M. E. Martins, C. F. Zinola and A. J. Arvia, *J. Braz. Chem. Soc.*, 1997, **8**, 363–370.

54 M. S. Rau, M. R. Gennero de Chialvo and A. C. Chialvo, *J. Power Sources*, 2013, **229**, 210–215.

55 W. T. Napporn, J.-M. Léger and C. Lamy, *J. Electroanal. Chem.*, 1996, **408**, 141–147.

56 T. E. Shubina and M. T. M. Koper, *Electrochimica Acta*, 2002, **47**, 3621–3628.

57 S. Motoo, M. Shibata and M. Watanabe, *J. Electroanal. Chem. Interfacial Electrochem.*, 1980, **110**, 103–109.

58 E. Christoffersen, P. Liu, A. Ruban, H. . Skriver and J. . Nørskov, *J. Catal.*, 2001, **199**, 123–131.

59 N. Furuya and S. Motoo, *J. Electroanal. Chem. Interfacial Electrochem.*, 1979, **98**, 195–202.

60 S. Mukerjee and R. C. Urian, *Electrochimica Acta*, 2002, **47**, 3219–3231.

61 J. Greeley, J. K. Nørskov and M. Mavrikakis, *Annu. Rev. Phys. Chem.*, 2002, **53**, 319–348.

62 S. C. S. Lai and M. T. M. Koper, *Faraday Discuss.*, 2009, **140**, 399.

63 A. Więckowski, *Electrochimica Acta*, 1981, **26**, 1121–1124.

64 G. Horányi and E. M. Rizmayer, *J. Electroanal. Chem. Interfacial Electrochem.*, 1986, **201**, 187–198.

65 J. K. Nørskov, J. Rossmeisl, A. Logadottir, L. Lindqvist, J. R. Kitchin, T. Bligaard and H. Jónsson, *J. Phys. Chem. B*, 2004, **108**, 17886–17892.

66 P. Zelenay, G. Horányi, C. K. Rhee and A. Wieckowski, *J. Electroanal. Chem. Interfacial Electrochem.*, 1991, **300**, 499–519.

67 A. Bach Delpeuch, M. Chatenet, C. Cremers and T. Tübke, *Electrochimica Acta*, 2014, **141**, 102–112.

68 U. Schmiemann, U. Müller and H. Baltruschat, *Electrochimica Acta*, 1995, **40**, 99–107.